Boundary-Layer Meteorology manuscript No.
(will be inserted by the editor)

Modelling Airflow over Pitched-Roof Buildings

Matthew Coburn · Zheng-Tong Xie · Steven J. Herring

Received: DD Month YEAR / Accepted: DD Month YEAR

Abstract Arrays of buildings with pitched roofs are common in urban and suburban areas of European cities. Nevertheless, while flows around flat-roof buildings have been well documented, the effect of pitched roofs has not. Large eddy simulations were used to predict the flows over flat and pitched-roof cuboids to gain a greater understanding of the impact of pitched roofs on urban boundary layers.The simulation methodology was first validated for an array of flat roof cuboids. Further simulations then showed that changes in the type of grid conformity had a negligible effect on the mean flow field and turbulent stresses, while having a visible, but small effect on the dispersive stresses for a given packing density. Comparisons were then made between the flowfields around flat roof cuboid arrays and pitched roof cuboid arrays at two different packing densities. Spatially averaged vertical profiles of time-averaged velocities, second order turbulent statistics, and dispersive stresses are presented, as well as spanwise and time-averaged profiles of surface pressure and pressure difference between the windward and leeward sides. Further work investigated the effects of turbulence level and stratification in the approaching flow. It is concluded that the interactions between pitched-roof buildings and their effect on the urban boundary layer are considerably different to those of flat-roof buildings. Importantly, it is also shown that in comparison to a flat roof array, the pitched roof one at a packing density 33% evidently increases the friction velocity and greatly reduces the effect of stable stratification conditions.

Keywords Pitched roof · Cartesian mesh · Thermal stratification · Packing density · Spatial-average · Drag coefficient

M. R. Coburn · Zheng-Tong Xie
University of Southampton
Southampton SO17 1BJ, UK
E-mail: mc6g16@soton.ac.uk; z.xie@soton.ac.uk

Steven J. Herring
AWE, Reading, RG7 4PR
E-mail: current address, Steve.Herring@awe.co.uk

1 Introduction

Past research in urban atmospheric problems has shown that coupling may exist between the boundary layer flowfields at City scale (O(10 km)), neighborhood scale (O(1 km)), and street scale (O(0.1 km)) (Barlow et al., 2017; Fernando, 2010). This spatial coupling effect is particularly strong around urban forms such as groups of tall buildings (Han et al., 2017; Fuka et al., 2018; Hertwig et al., 2019), or around steep topographic changes. To understand the importance of coupling effects we require a mapping between urban forms and flowfield characteristics, such as mean velocity, turbulent statistics, momentum and heat fluxes. Acquiring such data for the varied range of geometries encountered in urban areas challenges both numerical and experimental simulations in many aspects.

1.1 Buildings with Pitched Roofs

Most of the published experimental and numerical studies on idealized buildings (e.g. Cheng and Castro, 2002; Stoesser et al., 2003; Coceal et al., 2006; Xie and Castro, 2006) have focused on arrays of cuboid blocks with flat roofs, which are placed in an aligned or staggered arrangement with uniform or non-uniform heights. These studies are most relevant to urban flows over city centres where most of the buildings are likely to be cuboid in shape. However, in the surrounding urban and suburban areas of European cities most of the residential houses have pitched roofs. It is therefore of great interest to assess the effect of having pitched, rather than flat roofs, on the local flowfield and large-scale boundary layer flow.

There are a small number of published papers (Barlow et al., 2004; Yassin, 2011; Ferrari et al., 2016; Nosek et al., 2016, 2017; Llaguno-Munitxa et al., 2017; Badas et al., 2017; Woodward et al., 2021) in which different roof shapes and their effect on the flow field and dispersion has been investigated. Most of these studies (Barlow et al., 2004; Yassin, 2011) have investigated two-dimensional street canyons with various roof shapes. A few studies (Holmes, 1994; Tominaga et al., 2015; Ozmen et al., 2016; Fouad et al., 2018; Woodward et al., 2021) have also examined a single isolated building with a pitched roof and these have provided an understanding of the mean surface pressure (Ginger and Letchford, 1995; Oliveira and Younis, 2000; Tominaga et al., 2015) which has supported the development of building regulation codes.

Tominaga et al. (2015) have investigated the flow field and surface pressure on an isolated building for one aspect ratio and three roof pitch angles using particle image velocimetry (PIV) and computational fluid dynamics (CFD). They found large differences in the flow fields produced by the smaller and larger pitch angles, and suggested that a critical angle existed around the pitch angle 20°. Holmes (1994) found that a 30° pitched roof on a single tropical house had a considerable effect on the mean roof pressures. He found that the mean pressure coefficient on the upwind half of the roof was all positive, while on the leeward side the flow did not re-attach on the roof, resulting in a near uniform surface pressure. He also stated that roof pitches up to 10° with the wind normal to the ridge were "aerodynamically flat". These results suggest that modest changes in the angle of pitched roofs may have strong effects on the flowfield around the building and building surface pressures.

Fouad et al. (2018) also investigated isolated pitched-roof buildings to explore the potential for obtaining useful design data using CFD methods by comparing their results to the Eurocode and ASCE10 standards. They drew a conclusion, "the application of CFD techniques show great potential to offer very good wind design data for structures with shapes not listed in the existing codes." While building regulations are based on considering a single isolated building, it is probable that the flow within the canopy of an array of pitched roof buildings will be considerably different to that around an isolated building, with consequent effects on the surface pressure distribution. However, published studies on the effect of interference between buildings have typically only focused on two buildings (e.g. Bailey and Vincent, 1943; Holmes, 2007). Bailey and Vincent (1943) suggested that having a maximum of two buildings upstream of the instrumented model was sufficient to be representative of built up areas. Holmes (2007) concluded that the building spacing was a key parameter and the number of shielding rows was of lesser importance. This must be questionable though because only having two building rows upstream of the measurement location is insufficient to allow the internal boundary layer to become fully developed urban boundary layer (e.g. Hanna et al., 2002; Xie and Castro, 2008). For arrays of buildings placed in a fully developed turbulent rural boundary layer, it requires a fetch length of about ten average building heights. For arrays of buildings placed in a smooth laminar boundary layer, the required fetch length is much greater.

Two parameters frequently used to characterise the morphology of urban areas are the frontal and plan solidities (e.g. Placidi and Ganapathisubramani, 2015). The latter is more often termed the 'packing density' λ_p. The effect of packing density in arrays of simplified buildings with flat roofs has been intensively studied (e.g. Cheng et al., 2007; Placidi and Ganapathisubramani, 2015, 2018), and it has been shown that their total drag coefficient based on the freestream velocity is a function of the packing density. The drag coefficient function has minimums at $\lambda_p = 0$ or 100%, and a maximum in the lower half of the packing density range. Cheng et al. (2007) showed that the maximum drag coefficient was closer to $\lambda_p = 6.25\%$ than 25% for aligned arrays of cubes. There is a need to understand whether the drag coefficient function shows similar, or different, behaviour for arrays of blocks with pitched roofs. It must be noted though that the frontal solidity and packing density provide adequate descriptions of arrays for developing parameterisations for the effects of flat roofed buildings in meso-scale models, at least one further parameter is required to differentiate between arrays with different roof geometries.

1.2 Research Needs

The existing body of literature shows a clear need to investigate the effect of pitched roofs in building arrays at different frontal solidities, packing densities and aspect ratios with fetches sufficient to develop realistic urban boundary layers; to demonstrate improved methods for predicting the airflow and dispersion at neighbourhood scales; and to obtain spatially averaged momentum and scalar flux data which may be used to develop parameterisations for meso-scale models.

In addition to the above there is the question of thermal stratification effects in urban areas. These attracted little attention until one decade ago (Sessa et al.,

2018). The studies published since then have focused on arrays of idealised cuboid-shape buildings (e.g. Boppana et al., 2014; Kanda and Yamao, 2016; Tomas et al., 2016; Sessa et al., 2018; Marucci et al., 2018; Marucci and Carpentieri, 2020), or much simplified realistic buildings with flat roofs (e.g. Xie et al., 2013). They have concluded that even weakly stable stratification conditions (i.e. the bulk Richardson number ≤ 1) have a considerable impact on the urban boundary layer turbulence and significantly impacted pollutant dispersion.

To our knowledge there has been no research into the nature of the flow over arrays of pitched-roof buildings in thermally stratified conditions. The literature shows that a pitched roof can generate a very different flows within and above the canopy top in neutral stratification, with more three-dimensional flow structures than flows over flat-roof buildings. The question arises as to whether the effects of changes in thermal stratification are similar over pitched-roof buildings as over those with flat roofs.

With respect to producing numerical simulations of the flow around buildings it is the case that rather than using conformal meshes to accurately capture the geometric details of buildings (such as pitched roofs), two widely used urban CFD codes PALM-4U (Maronga et al., 2020; Krč et al., 2020) and DALES-Urban (Heus et al., 2010; Grylls et al., 2020) use non-conformal cartesian meshes. This simple treatment is attractive as it leads to significant improvements in computational efficiency, but raises the question of what the penalty in accuracy is compared to using conformal (body fitted) meshes? This question is also addressed by the study.

1.3 Outline of Current Work

This study aims to address three knowledge gaps: 1) how the urban boundary layer is affected by having an array of buildings with pitched roofs, 2) how the effect varies with the packing density of the array, and 3) how the effect changes as the conditions vary from neutral to stable stratification.

Section 2 presents details of the numerical methods, Section 3 describes the cases and simulation settings. Section 4 details the verification and validation of the CFD model. Section 5 examines the effect of using conformal and non-conformal meshes, Section 6 presents a comparison between arrays of building blocks with and without pitched roofs, which includes spatially-averaged velocities, Reynolds stresses and surface pressure. Section 6.2 reports the effect of packing density in neutral stratification. Section 7 reports the stratification effects on flow over pitched-roof buildings. Section 8 raises a discussion associated to Eurocode on pitched roofs. Section 9 summarises the conclusions from the research undertaken.

2 Numerical Methods

2.1 Governing Equations

The flow which develops over arrays of blocks is innately unsteady and so is best resolved by adopting a large eddy simulation (LES) approach (e.g. Kanda et al.,

2004; Xie and Castro, 2006; Castro, 2017). Equations 1 and 2 are respectively the filtered continuity and Navier-Stokes equations for large eddy simulations (LES):

$$\frac{\partial u_i}{\partial x_i} = 0 \tag{1}$$

$$\frac{\partial u_i}{\partial t} + \frac{\partial u_i u_j}{\partial x_j} = -\frac{1}{\rho}\frac{\partial p}{\partial x_i} + \nu\frac{\partial^2 u_i}{\partial x_j \partial x_j} - \frac{\partial \tau_{ij}}{\rho \partial x_j} - \frac{1}{\rho}\frac{\partial P}{\partial x_i}\delta_{i1} + f\delta_{i3}, \tag{2}$$

where u_i and p are the resolved or filtered velocity and pressure respectively, τ_{ij} is the Subgrid-scale (SGS) stress. δ_{i1} is the Kronecker-delta and $\frac{\partial P}{\partial x_i}$ is the pressure gradient or body force term which drives the flow while periodic boundary conditions are used in LES. $f\delta_{i3}$ is the body force in the vertical direction due to thermal buoyancy and is calculated by using the Boussinesq approximation based on the estimated temperature in Eq. 3. The mixed time scale SGS model (Inagaki et al., 2005) was used to avoid using near wall damping functions as used in the Smagorinsky SGS model. Nevertheless, it was suggested in Xie and Castro (2006) that the flow is very much building block-scale dependent that the results are not-sensitive to the precise nature of the SGS model, subject to a requirement that the grid sufficiently resolves the inertial range of the turbulent spectra.

The filtered transport equation of temperature is:

$$\frac{\partial T}{\partial t} + \frac{\partial u_j T}{\partial x_j} = \frac{\partial}{\partial x_j}\left[(D + D_r)\frac{\partial T}{\partial x_j}\right], \tag{3}$$

where T is the resolved-scale temperature. D is the molecular diffusivity of temperature, D_r is the SGS diffusivity and is given by ν_r/Pr_r, where ν_r is the SGS kinematic viscosity, Pr_r is the subgrid Prandtl number set to 0.9.

2.2 Setting of Thermal Stratification

In this study thermal stratification effects are set by using the bulk Richardson number, which offers a convenient approach for quantifying the strength of stratification due to the vertical temperature gradient in numerical simulations. The bulk Richardson number is defined as:

$$Ri = \frac{g\delta(\overline{T}_{\mathrm{ref}} - \overline{T}_0)}{\overline{T}_0 \overline{U}_\infty^2}, \tag{4}$$

where g is acceleration due to gravity, δ is the domain height, $\overline{T}_{\mathrm{ref}}$ is the mean ground temperature, $\overline{T}_0$ is the mean freestream temperature and $\overline{U}_\infty$ is the mean freestream velocity at the inlet.

2.3 Boundary Conditions

The LES model must be used with boundary conditions which are appropriate to the problem. For urban flow simulations the inflow and outflow faces typically have periodic boundary conditions (PBC) (e.g. Coceal et al., 2006) or synthetic turbulence inflow conditions (STI) (e.g. Xie and Castro, 2008). An LES simulation

with PBC is based on the assumption that the simulated domain is a repeat unit of a much greater region. This approach can substantially reduce the computational cost. However, when modelling a 'real' urban geometry, the PBC approach could lead to an inaccurate representation of the flow in some scenarios, because as stated in Xie and Castro (2009) the repeat unit creates wakes that impact itself.

The synthetic turbulence inflow (STI) method has been well documented (Xie and Castro, 2008; Sessa et al., 2018) and simulations using it have compared very well to data from experiments (Marucci et al., 2018; Marucci and Carpentieri, 2020). STI requires vertical profiles of mean velocity, Reynolds stresses, and integral length scales as inputs. To apply thermal stratification at the inlet STI requires vertical profiles of mean temperature, and the variance and integral length of temperature fluctuations as additional inputs.

In this paper, we use the PBC and STI boundary conditions for two different sets of simulation cases. The choice of boundary conditions was driven by the physics to be simulated and so STI boundary conditions were used for examining the effect of thermal stratification. So that the results could be compared with past work on block arrays with flat roofs, the same STI inputs were used for the thermal stratification cases as in Sessa et al. (2020). This meant that the prescribed vertical profiles of mean velocity, Reynolds stresses, mean temperature and temperature fluctuations for simulating $Ri = 0,\ 0.2,\ 0.5$ and 1 were identical to those used in Sessa et al. (2018), which matched the experimental data in Marucci et al. (2018). It should be noted that the same prescribed inflow data were used for $Ri = 0.2,\ 0.5$ and 1. This was because as stated in Sessa et al. (2018), using the same settings allows the effect of thermal stratification to be isolated for investigation.

2.4 Spatial Averaging

The spatial averaging method was adopted for processing the outputs from all the simulations. In particular, the comprehensive spatial average (Xie and Fuka, 2018) was selected. This takes account of the output quantities having zero values in solid regions, while the solid regions within the domain are included in the total volume. Equation 5 defines the comprehensive spatial average:

$$\langle\phi\rangle_c(z) = \frac{1}{S_c}\int_{(S_f)} \phi(x,y,z)\mathrm{d}x\mathrm{d}y, \tag{5}$$

where $\langle\rangle$ denotes spatial average, ϕ denotes the quantity to be spatially-averaged, S_c and S_f respectively denote the total area and the fluid area on a height z.

The comprehensive spatial average has the advantage that it produces a smooth change of total momentum flux across the canopy interface (Xie and Fuka, 2018). In comparison, the intrinsic spatial average which only includes the fluid regions in the averaging leads to a discontinuity in total momentum flux at the canopy height. The fact that the comprehensive spatial average gives a smooth change in momentum flux is potentially advantageous in developing a parameterization of momentum flux, or other quantities, for a meso-scale model.

3 Details of Cases Studied

3.1 Array Geometries

The idealized-morphology studied here takes the form of a simplified urban-like geometry. Arrays of simple shape blocks, i.e. cuboids with either flat or pitched roofs, are studied. The baseline cuboid has dimensions 2H x 1H x 1H, where $H = 1m$. The Reynolds number based on the block width H and the velocity at height H in the upstream boundary layer is abut 7400, or about 830 based on the friction velocity u_τ, which is estimated using an extrapolation from the linear turbulent shear stress profile above the canopy (e.g. Fig. 6).

Two different packing densities (i.e. λ_p= 33.3% and 16.7%) are simulated. The baseline flat roof cases of height H were validated against Castro et al. (2017). Further cases of height $1.5H$ with a flat roof or a 45° pitched roof, were then compared to the baseline case. Figure 1 shows the geometries of the three different blocks used and diagrams illustrating the packing densities.

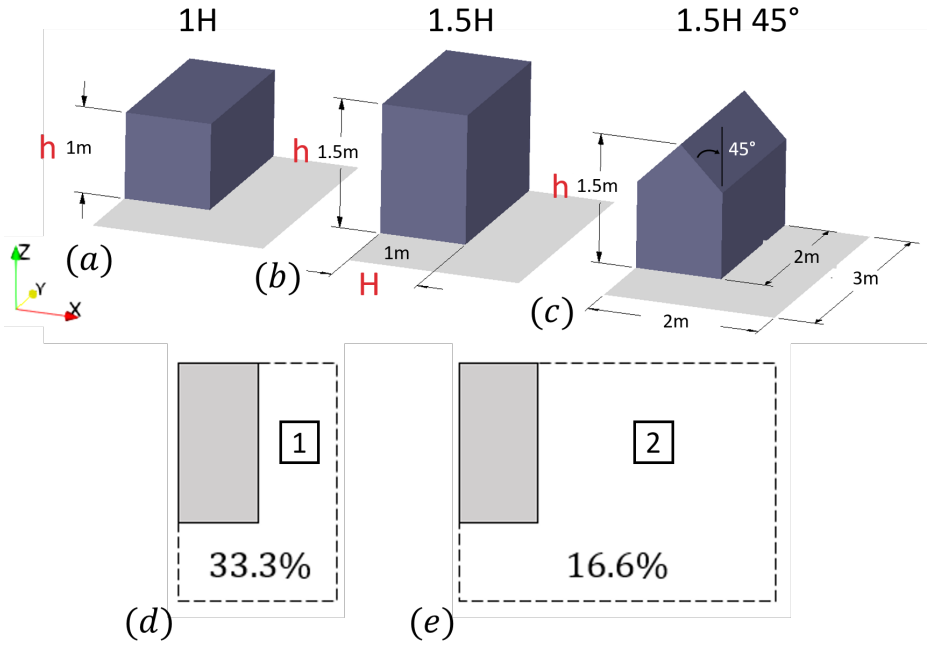

Fig. 1: Diagram of the smallest repeat unit size for a) 1H, b) 1.5H, c) 1.5H 45° pitched roof, with the same plan view and packing density, λ_p= 33.3%. H, the block width. h, the block height. x coordinate is perpendicular to the long side of the cuboid and the long street, and z coordinate is in the vertical direction, d) packing density λ_p= 33.3% (as in Fig.1), e) packing density λ_p= 16.7% where the width of the long street marked with "2" is tripled compared to "1" in d)

3.2 Meshes and Test Cases

The meshes used in this study were created using SnappyHexMesh which is far more flexible and efficient than standard structured-mesh generators. It was used to assess its suitability for application to much larger domains in follow-on studies. This study utilised the capability of SnappyHexmesh to create uniform grids, grids with multiple levels of resolution and non-conformal and conformal meshes.

For the baseline flat-roof cases uniform cartesian grids (identified as (U)) were first created with a resolution of $H/16$. This was in accordance with the minimum level of resolution suggested in Xie and Castro (2006) and Coceal et al. (2006). Further cartesian meshes were then created with three levels of grid resolution (identified as (3R)) aa used in Xie and Castro (2006). These had a resolution $H/16$ up to $z = 2.5H$, a resolution $H/8$ between $z = 2.5H$ and $z = 8.5H$, and finally a resolution $H/4$ from $8.5H$ up to the top of the domain at $12H$.

All the Cartesian meshes created for the flat roof cases were conformal. However, if a simple Cartesian mesh is created for a pitched roof, the mesh is non-conformal as shown in Fig. 2. To address the question of what impact this has, three meshing strategies were used for the pitched-roof cases: uniform conformal-grids (UC), Uniform non-conformal grids (UNC) and a 3-level resolution-conformal grid (3RC).

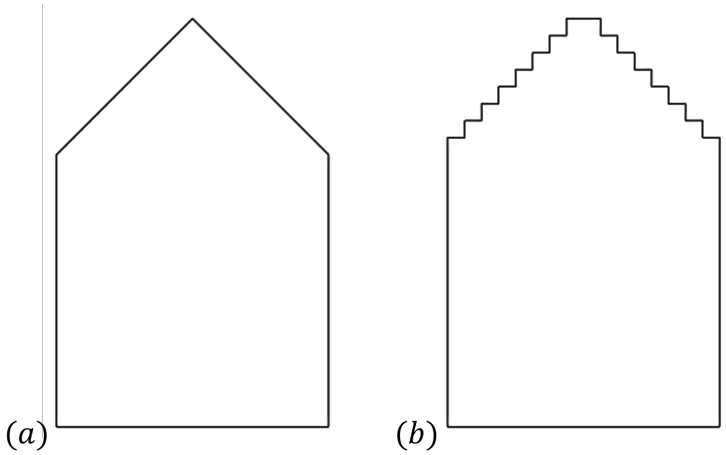

Fig. 2: Side view of the surface meshes of pitched-roof cuboids of a) conformal mesh, 1.5H 45°(UC, 3RC) and b) non-conformal mesh, 1.5H 45°(UNC)

The majority of the cases were run at neutral stability conditions with PBC at the inflow and outflow. For these cases the domain had dimensions of $12H$x$12H$x$12H$, as shown in Fig. 3(a). For the cases with thermally stratified inflows, the STI boundary condition was applied. The domain was sized to match that used in Sessa et al. (2018), which was $31.5H$ x $12H$ x $12H$ shown in Fig. 3(b). In both cases periodic boundary conditions were applied to the spanwise boundaries, and a stress free condition was set for the top boundary.

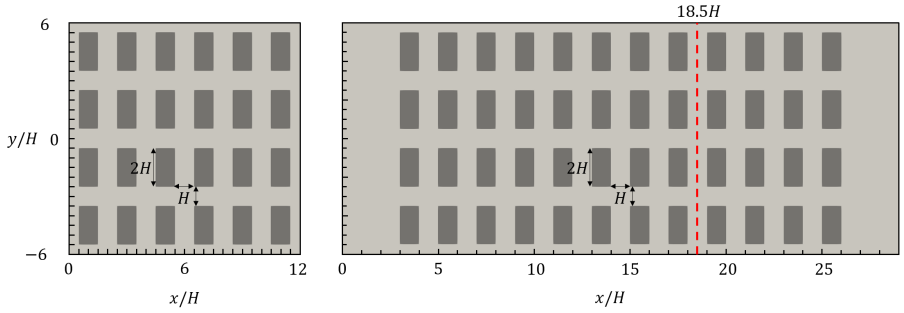

(a) (b)

Fig. 3: Plan view of the two domains with a packing density λ_p= 33.3%. (a) The PBC domain. (b) The STI domain. Removing every other column of cuboids in (a) results in λ_p= 16.7%. Red dashed line denotes where laterally averaged vertical profiles are presented

Table 1 summarises the neutral stability cases simulated with the baseline packing density of 33.3%. Table 2 summarises the cases run to examine the effect of changing the packing density from 33.3% to 16.7%. Table 3 summarises the cases run to examine the effect of thermal stratification on the flow over arrays of packing density 33.3%.

Table 1: Outline of different cases for uniform cuboid arrays with different heights, roof-shapes and packing densities in various thermal stratification conditions

Cuboid Arrays	**Canopy height (m)**	**Roof, Grid Description**
1H (U)	1	Flat, Uniform grid
1H (3R)	1	Flat, 3 Level grid
1.5H (U)	1.5	Flat, Uniform grid
1.5H (3R)	1.5	Flat, 3 Level grid
1.5H 45° (UC)	1.5	Pitch, Conformal uniform grid
1.5H 45° (UNC)	1.5	Pitch, Non-Conformal uniform grid
1.5H 45° (3RC)	1.5	Pitch, Conformal 3 Level grid

Table 2: Cases for packing densities of 33.3% and 16.7%

Cuboid Arrays	**Packing Density(λ_p)**	**Roof, Grid Description**
1H, 1.5H, 1.5H 45° (3RC)	16.7%	Flat/Pitched, 3 Level grid
1H, 1.5H, 1.5H 45° (3RC)	33.3%	Flat/Pitched, 3 Level grid

Table 3: Thermal stratification cases

Stratified Cases	**Richardson Number(Ri)**	**Roof, Grid Description**
1.5H (UCI)	0, 0.2	Flat, Conformal, Inflow turbulence
1.5H 45° (UCI)	0, 0.2, 0.5, 1	Pitched, Conformal, Inflow turbulence

4 Validation of Flow Simulation around Cuboid Array

To validate the methodology simulations were first made of cases cases 1H(U) and 1H(3R) with $\lambda_p = 33.3\%$ and PBC. Figure 4 shows that within the canopy the differences of the mean streamwise velocity and Reynolds stresses between the cases 1H(U), 1H(3R) and the LES data in Castro et al. (2017) are negligible in the centre of the long street location on the lee side of the block marked "1" in Fig. 1d. The mean velocity profiles at all locations (not shown) agreed very well with those in Castro et al. (2017). The street canyon flow was captured very well, with both cases precisely resolving the reversed flow. The turbulent fluctuation rms profiles of the uniform mesh case 1H(U) agreed well with Castro et al. (2017) over the entire vertical extent. The Reynolds stresses within the canopy for case 1H(3R) had a maximum difference of 5% compared to those for case 1H(U) and Castro et al. (2017). This was due to the coarser resolution above the canopy in case 1H(3R). We consider a maximum difference of 5% to be acceptable as the differences immediately above the canopy were very small. Figure 4 suggests that the domain height was sufficient as there are no effects on the profiles close to the top boundary.

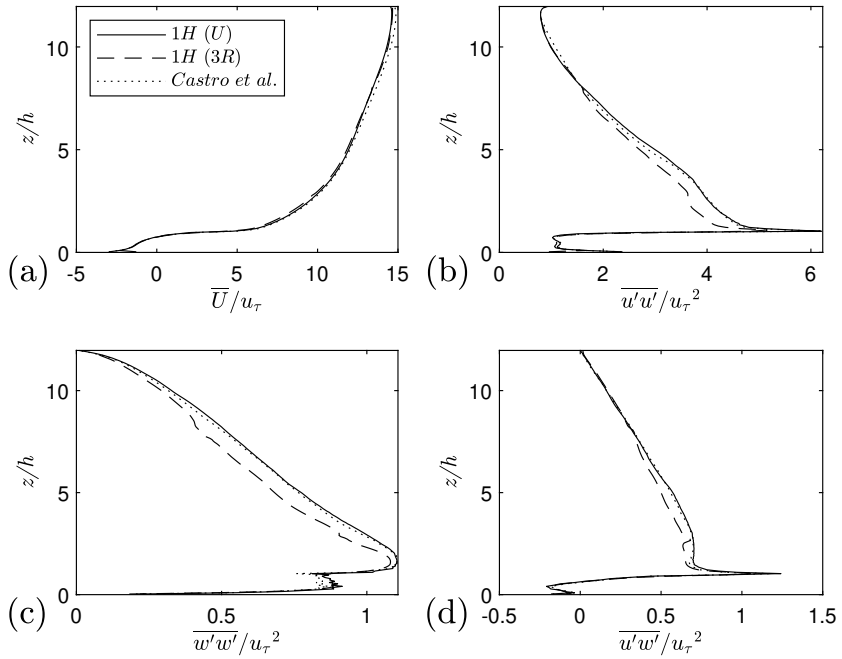

Fig. 4: Comparison between cases 1H(U), 1H(3R) and Castro et al. (2017) data at long street location "1" marked in Fig. 1d. a) axial mean velocity, b) streamwise normal stress, c) vertical normal stress, d) Reynolds shear stress

The Reynolds stress profile in Fig. 4d for the case 1H(3R) exhibits a small disturbance at $z/h = 2.5$ and $z/h = 8$, due to the change of grid resolution. In summary, the comparison suggested that the conformal (body fitted) grids produced using SnappyHexMesh for cases 1H(U) and 1H(3R) led to results in agreement to those obtained in Castro et al. (2017). This provided the validated baseline from which to conduct the remainder of the study.

5 Impact of Using Conformal or Non-Conformal Meshes

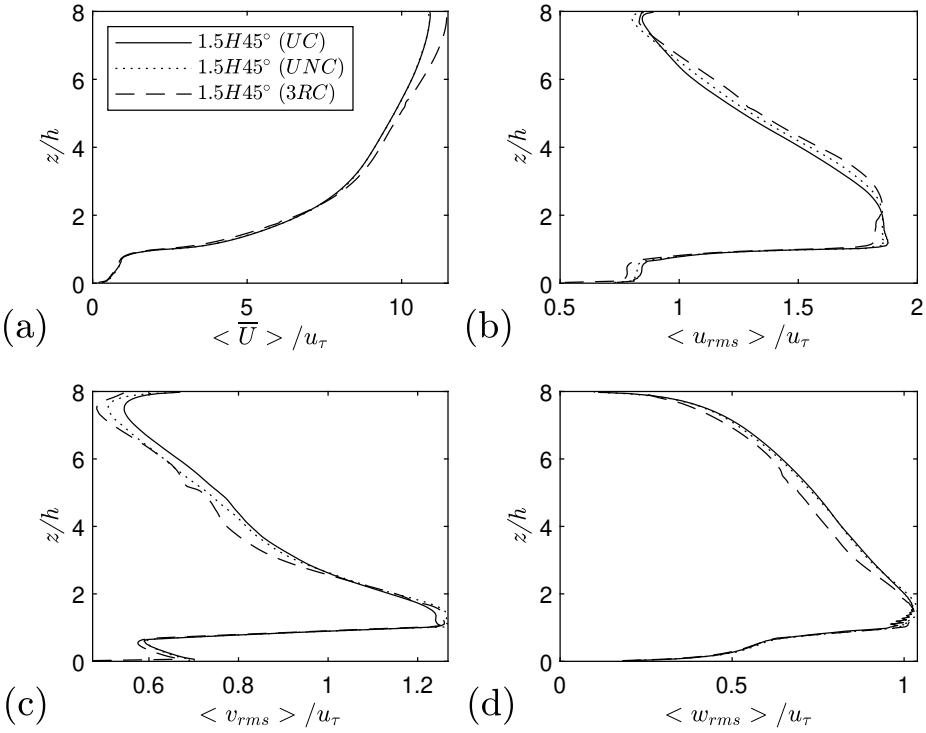

Fig. 5: Grid and geometry effects on a) spatially averaged streamwise mean velocity, b) axial velocity fluctuation *rms* c) spanwise velocity fluctuation *rms* and d) vertical velocity fluctuation *rms*. All normalised by u_τ

This section examines the effect of having conformal or non-conformal grids on the flow predictions obtained for a block array with pitched roofs. This is done be comparing spatially averaged profiles for the 1.5H 45° (UC), 1.5H 45° (UNC) and 1.5H 45° (3RC) cases at a packng density of 33.3% with PBC.

Figure 5 shows that all three cases produced consistent vertical profiles of mean streamwise velocity and *rms* velocity fluctuation components. Overall agreement between the three cases is promising, especially for the mean velocity profile in Fig. 5a. All cases predict similar peak *rms* velocity fluctuations with diffrences of less than 5% within and above the canopy.

At the top of the domain, the increases in axial and particularly spanwise turbulence intensities are due to the so-called 'splatting' of the eddies on the top boundary, where the vertical velocity is constrained to be zero. This is not important becasue as disussed in Xie et al. (2008) the domain height is great enough to avoid any top boundary condition effect on the regions of interest, i.e. within and immediately above the canopy. It can be seen that at $z/h = 2$ where the interface between the $H/16$ and $H/8$ grid regions occurs, the axial fluctuating

velocity rms peak in Fig. 5b and a Reynolds shear stress peak in Fig. 6a are visible. These only have a very local effect and don't evidently impact the flow regions within and immediately above the canopy.

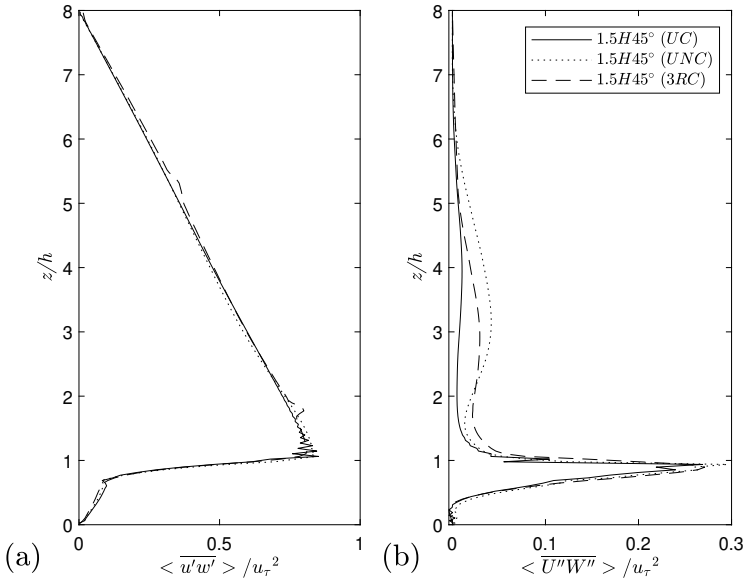

Fig. 6: Grid effects for array of cuboids $\lambda_p = 33.3\%$ with 45° pitched roofs a) spatially averaged Reynolds stress and b) spatially averaged dispersive stress.

Figure 6 shows spatially averaged vertical Reynolds stress and dispersive stress profiles. There are negligible differences between the three cases within the canopy. The peak dispersive stress occurs just below the canopy top for the three cases. The 1.5H 45°(UNC) case with non-conformal grid and 1.5H 45°(3RC) case with coarse grid above the canopy produce a small but visible discrepancy (less than 0.05) from height $z/h = 2$ to $z/h = 5$, compared to the case 1.5H 45°(UC). The visible differences in the dispersive stress profile between a conformal and non-conformal grid could throw into question the use of a non-body fitted grid, such as adopted by the PALM (Maronga et al., 2020) and DALES (Heus et al., 2010) codes, especially when considering suburban neighbourhood scale simulations.

We speculate that the inaccurate representation of the local flow details in the vicinity of the pitched roof in the non-body fitted grid case 1.5H 45°(UNC) could affect the prediction of local skin friction and other flow parameters. Nevertheless, Figures 5 and 6 suggest that the overall discrepancy between the spatially averaged mean velocity, Reynolds stresses and dispersive stresses due to using a non-corformal rather than a conformal grid is small.

Figure 6a shows a linear decrease in Reynolds shear stress from the canopy top, reducing to zero at the domain top. The non-dimensional total shear stress (not shown) including the drag due to the blocks linearly increases within the canopy to almost 1 at the ground. This is expected because a constant body force $\frac{\partial P}{\partial x}$ is set to drive the flow, and confirms the high accuracy of the simulations (see Xie

and Fuka, 2018). The mesh resolution and numerical settings for the flat roof cases are validated in Sect. 4, and are kept the same for the pitched roof cases. All these ensure reliable results for the pitched roof cases.

6 Comparison of the Turbulence Statistics and Aerodynamics of Flat and 45° Pitched Roofs

This section compares flow fields, turbulence statistics, surface pressure coefficients and drag coefficients between arrays of cuboids with flat and 45° pitched roofs. It aims to provide an understanding of how having a pitched roof affects these quantities and thereby to quantify the importance of accurately accounting for the impact of pitched roofs on the boundary layer flow.

Two packing densities $\lambda_p = 16.7\%$ and 33.3% of uniform cuboid arrays with and without pitched roof were simulated. Spatially-averaged mean velocities and Reynolds stress profiles were examined to understand the combined effects of a pitched roof and packing density.

6.1 Effect of Pitched Roof on Urban Canopy Flows

It is known that a ratio of the building height to the boundary layer thickness $h/\delta \approx 1/10$ yields a negligible effect on the flow and turbulence within and above the canopy (e.g. Coceal et al., 2006; Xie et al., 2008). It is worth identifying any differences of flow and turbulence over pitched-roof and flat-roof buildings in a thick boundary layer. Figure 7a shows a comparison of the spatially averaged vertical profiles of axial mean velocity between the pitched roof case 1.5H 45°(UC), and the flat roof cases 1.5H(U) and 1H(U), in which the vertical coordinate is normalized by the canopy height h, and the profiles of rms velocity fluctuation components are normalised by the friction velocity u_τ. Within the canopy there are only small differences between the three cases, as they are of the same packing density λp=33.3%. The two flat roof cases show a much greater inflection of mean streamwise velocity at the canopy height (Fig. 7b), which is associated with an overall "smoother" canopy top resulting a weaker shear immediately above the canopy, compared to the pitched roof case. The pitched roof generates far more drag on the flow. This can be seen from the more retarded velocity profile in Fig. 7a, and from the values of normalised friction velocity in Table 4. We now examine the flowfields in detail to understand the reasons for this.

Table 4: Normalised friction velocity for each case for packing densities, $\lambda_p = 33.3\%$ and $\lambda_p = 16.7\%$. $U_{3h}$is the mean streamwise velocity at $z = 3h$

Case	λ_p	u_τ/U_{3h}
1H(UC)	33.3%	0.0995
1.5H(UC)	33.3%	0.0928
1.5H 45°(UC)	33.3%	0.1207
1H(3RC)	16.7%	0.133
1.5H(3RC)	16.7%	0.132
1.5H 45°(3RC)	16.7%	0.130

Figure 8c shows that the shear layer at the canopy top impinging on the windward pitched roof for this packing density, resulting in far higher vertical mean velocity magnitude (not shown) and vertical velocity fluctuations Fig. 7d, and could be considered similar to a random height array (Xie et al., 2008), which produces greater drag and turbulence mixing as well (than uniform height blocks with flat roof). The axial, spanwise and vertical velocity fluctuation rms data are shown in Fig. 7b, c and d respectively. Within the canopy, the dimensionless rms velocity fluctuations are significantly different. The behaviour of the vertical profiles for the two flat roof cases are similar above the canopy, whereas the deeper canopy evidently suppresses the turbulent fluctuations of all three components within the canopy. The pitched roof alters the behaviour of the vertical profiles significantly above the canopy.

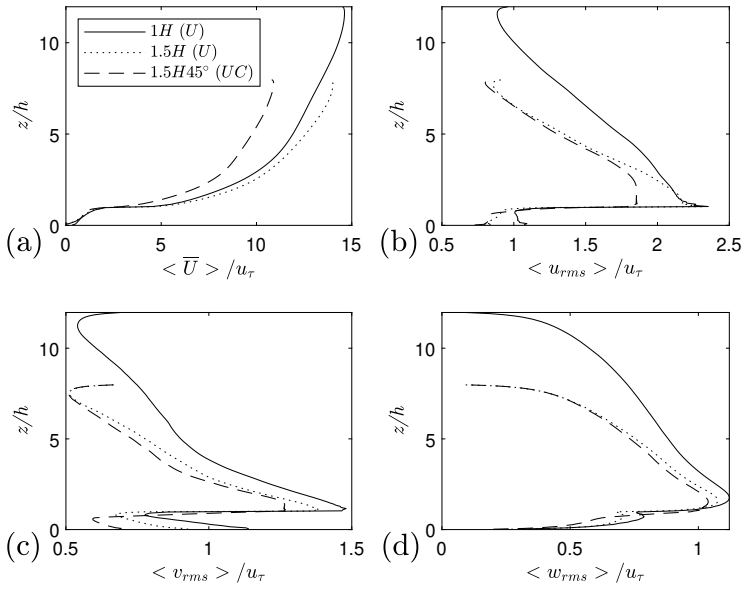

Fig. 7: Comparison of the spatially averaged vertical profiles between flat roof and pitched roof. a) streamwise mean velocity $\bar{U}$, b) u_{rms}, c) v_{rms} and d) w_{rms}

Figure 8 (a,b,c) shows mean ensemble average flow field vector plots of the street canyon in the $x-z$ plane up to a height of z/H=2 for the 1H(U), 1.5H(U) and 1.5H 45°(UC) cases respectively. The differences in flow pattern are evident. Fig. 8a and b for the flat roof cases show skimming flow regimes, whereas Figure 8c for the pitched roof exhibits a flow in the wake interference regime. From the surface pressure and skin friction data, we noticed that the flow stagnation occurs at $z/h = 0.94$ for the flat roof cases, and at $z/h = 0.8$ for the 1.5H 45°(UC) case.

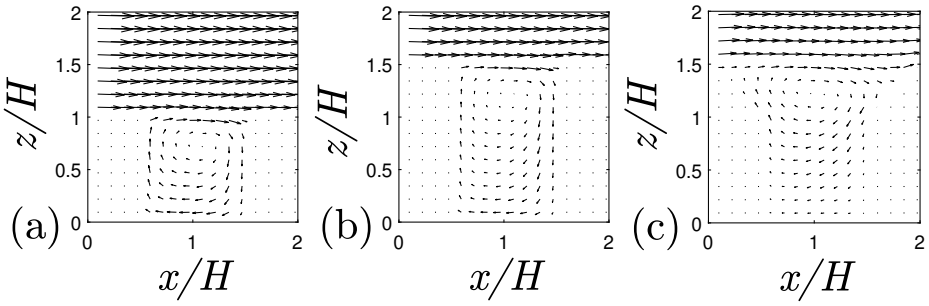

Fig. 8: Mean ensemble average velocity vector plot across the x,z plane in the centre of the long street for a) 1H(U), b) 1.5H(U) and c) 1.5H 45°(UC)

The observations above are reinforced by Fig. 9 which shows very different normalised instantaneous axial velocity contours for the 1.5H flat and pitched roof cases. The flat roof creates an obvious interface at the canopy top, where a thin shear layer forms; whereas the pitched roof generates a far thicker shear layer from the apex of the roof, and a less visible interface. Vorticity contours (not shown) for both cases show the same phenomenon.

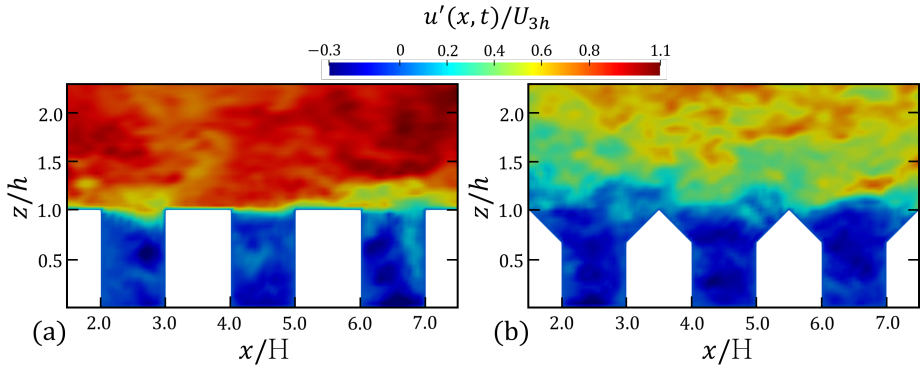

Fig. 9: Normalised instantaneous streamwise axial velocity contour across $x - z$ plane on the centre of the long street for a) 1H(U), b) 1.5H(U) and c) 1.5H 45°(UC)

Fig. 10 shows how the pitched roof changes the spanwise flow around the cuboid. The development of the secondary flows evident in Fig. 10(a) and (b) has been well documented for uniform height flat-roof cuboids with various aspect ratios (Willingham et al., 2014; Vanderwel and Ganapathisubramani, 2015; Tomas et al., 2017). However, the pitched roof effectively destroys any secondary flow Fig. 10(c). This is due to the large mean upwards flow at the apex of the roof, which is largely uniform across the span. The pitched roof also greatly enhances the axial rotation seen at the corner of the apex.

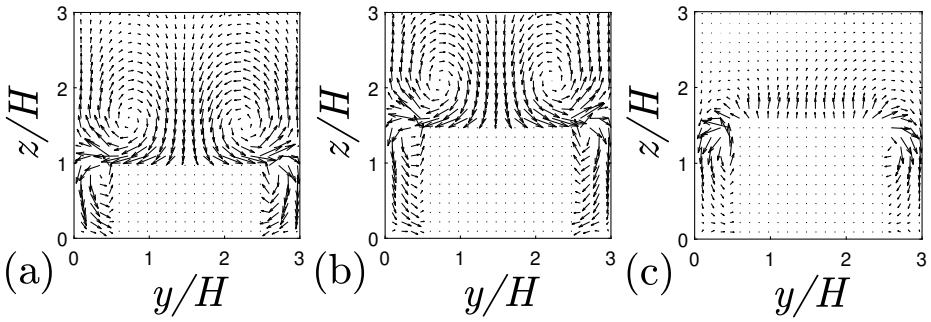

Fig. 10: Mean ensemble average velocity vector plot across the y,z plane in the centre of the cuboid for a) 1H(U), b) 1.5H(U) and c) 1.5H 45°(UC)

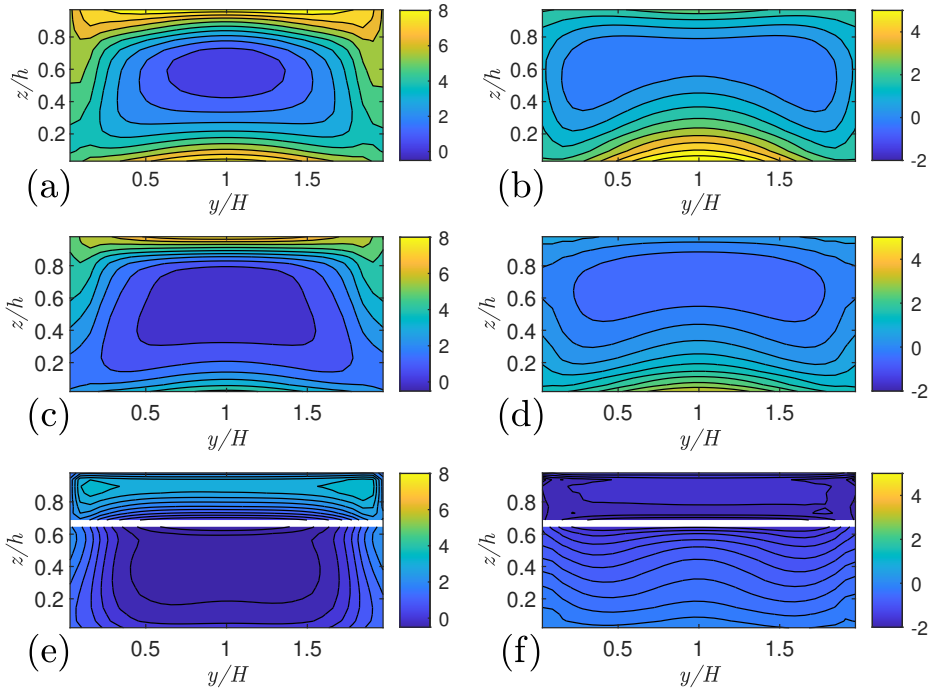

Fig. 11: Surface pressure contours normalised by ρu_τ^2. a) 1H(U) windward, b) 1H(U) leeward, c) 1.5H(U) windward, d) 1.5H(U) leeward, e) 1.5H 45°(UC) windward, f) 1.5H 45°(UC) leeward. White band denotes the roof-wall joint

Figure 11 shows pronounced differences in the windward and leeward surface pressure distributions normalised by ρu_τ^2 on the three blocks. The windward side plots show similar pressure distributions for both the flat-roof cases, 1H(U) and 1.5H(U) (Fig. 11a and c respectively).The pitched-roof case, however, shows a

considerably different surface pressure distribution. The vertical face from $z = 0$ to $2h/3$ shows a similar low pressure region to the two flat roof cases, but with a lower pressure which extends much deeper into the canopy and further across the span.

On the leeward side similar distributions are again observed for the flat-roof cases (Fig. 11b and d). But the leeward side of the pitched roof case (Fig. 11e) displays a much more uniform distribution across the span, due to the more uniform mean flow across the span shown in Fig. 10(c).

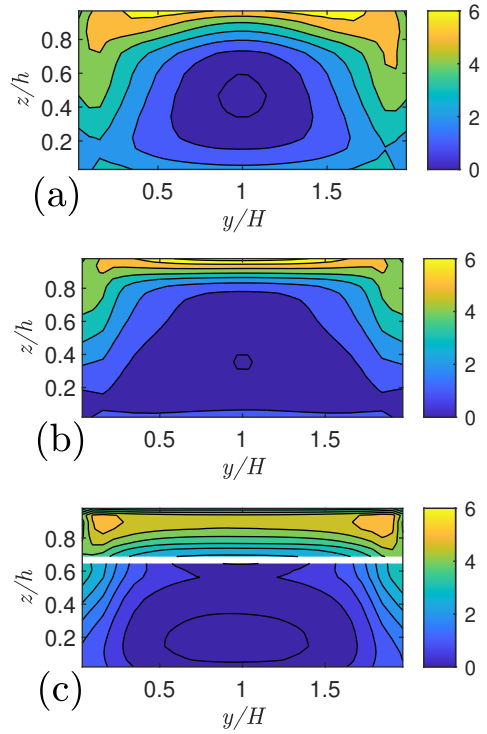

Fig. 12: Contours of pressure difference between the windward and leeward sides normalised by ρu_τ^2. a) 1H(U), b) 1.5H(U), c) 1.5H 45°(UC)

Figure 12 shows contours of pressure difference between the windward and leeward sides for the three cases 1H(U), 1.5H(U), and 1.5H 45°(UC). This figure show a similar surface pressure difference distribution as that in Tsutsumi et al. (1992) with the highest volume ratio (packing density). The data collected also follows the same pattern that, the surface pressure difference goes from low to high from the centre span to edge. The pressure difference peak occurs at $y = 0$ and almost the canopy top for the flat-roof block, whereas the pressure difference peaks on the pitched roof occurs at $y/H = 0.15$ and 1.85, and $z/h = 0.9$. The pressure difference on the pitched roof shows a high uniformity across the span,

which is likely again owing to a dominant flow along the roof surface towards the apex of the roof.

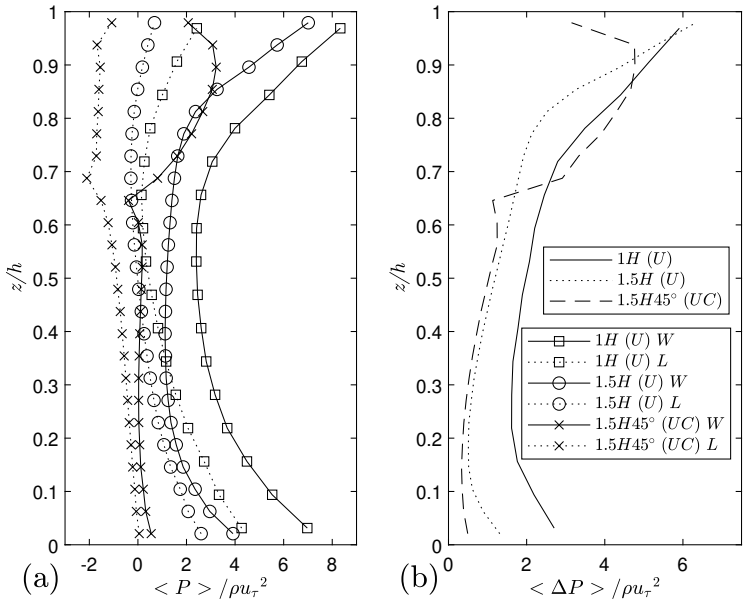

Fig. 13: Comparison of vertical profiles of a) spanwise averaged surface pressure on windward (W) and leeward (L) sides, and b) pressure difference between windward and leeward sides

Figure 13a shows vertical profiles of spanwise averaged surface pressure on windward and leeward sides. The profiles for two flat cases are similar in shape. The pitched roof creates significantly different profiles in shape above $z = 2h/3$. A noticeable inflection is present at the transition between side and roof, which occurs at slightly different vertical locations on windward and leeward sides, this is likely due to not having data on the transition point. The maximum surface pressure at $z/h = 0.9$ on the windward side, denotes the stagnation. Stagnation is not visible on the windward sides of the flat-roof cuboids, which occurs too close to the canopy top to be resolved in the current mesh. Figure 13b shows normalised spanwise-averaged pressure difference. A considerable difference is shown between the flat-roof case 1.5H(U) and the pitched-roof case 1.5H 45°(UC) above $z = 2h/3$. The pressure difference exhibits a similar inflection occurring $z = 2h/3$ as in Fig. 13a, accompanied by an abrupt increase in the pressure difference above $z = 2h/3$, which peaks at $0.9h$ and decreases towards the canopy top. The 1.5H(U) case exhibits a lower pressure difference across the depth of the canopy, compared to the shorter cuboid case 1H(U). A sharp increase occurs above $z = 0.8h$ for the 1.5H(U) case, and one occurs above $z = 0.7h$, which are consistent with the pressure profiles on the windward sides for the respective flat-roof cases in Fig. 13. These changes in shape are likely associated to the heights of the recirculation centres within the long street shown in Fig. 10a and b.

Figure 14a shows dimensionless spatially-averaged Reynolds shear stress profiles. Within the canopy the pitched roof generates far less Reynolds shear stress. The profiles for the two flat roof cases are similar, with the lower cuboid case generating slightly more Reynolds shear stress within the canopy. When focusing on the flow immediately above and within the canopy, it is more appropriate to normalise quantities by the friction velocity. The friction velocity normalised by the free stream velocity of the pitched-roof cuboid array is much greater, $u_\tau/U_\infty = 0.37$, around 25% larger than the $1.5H$ flat roof case, $u_\tau/U_\infty = 0.28$, and around 30% larger than the the $1H$ flat roof case, $u_\tau/U_\infty = 0.26$. Table 4 shows more details of u_τ/U_{3h}, where U_{3h} is the mean streamwise velocity at $z = 3h$. When focusing on the flow far above the canopy, it is more appropriate to normalise the flow quantities by the free stream velocity U_∞, or the velocity high above the canopy e.g. $z = 3h$. We noticed that the peak Reynolds shear stress normalised by U_{3h} is about 100% higher for the pitched roof case (not shown), suggesting that the pitched roof vastly increases the drag, mixing and re-entrainment of the flow into the canopy. Within the canopy, Reynolds shear stress normalised by U_{3h} shows the same behaviour to that normalized by the friction velocity u_τ. Considering only the packing density $\lambda_p = 33.3\%$ against a flow region map based on flat-roof data, the flows fall into the the skimming region. However, the entrainment into the street canyon is less-energetic due to the pitched roof because the mean flow in the shear layer has a non-negligible upwards component and some portion of flow is directed upwards instead of into the street canyon. Taking account of this, the flow over the pitched-roof array with $\lambda_p = 33.3\%$ falls into the wake interference regime.

The pitched roof creates a more uniform mean flow field across the span of the cuboid. The local peak Reynolds shear stress differs less than 7% across the span of the cuboid at the long street location, i.e. station "1" in Fig. 1, with a maximum occurring at the center of the span. The flat roof cuboid generates the maximum Reynolds shear stress at $0.1h$ from the spanwise edge of the cuboid.

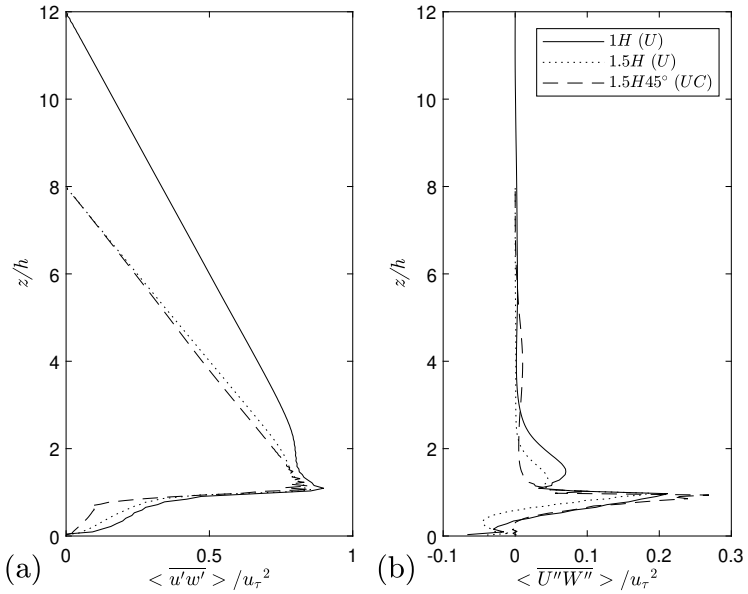

Fig. 14: Spatially-averaged profiles of a) dimensionless Reynolds shear stress, b) dimensionless dispersive stress

Figure 14b shows spatially-averaged vertical dispersive stress profiles, which are the mean flow contributions to vertical momentum flux. The pitched roof creates significantly larger dispersive stresses at the canopy height compared to the flat roof - it is to be noted the friction velocity u_τ is much greater for the pitched roof case. At $z = 2h$ and $1.5h$, the flat roof cuboids generate larger dispersive stresses, whereas the pitched roof generate negligible dispersive stress at the same height. We speculate that the pitched roof generates more turbulent fluctuations and mixing at the canopy height resulting in less mean flow variations.

6.2 Packing Density Effects Accounting for Roof Shape

Figure 15 shows spatially-averaged mean streamwise velocity and Reynolds shear stress profiles for the three block geometries at packing densities of 33.3% and 16.7%. With the exception of the 1.5H45°(3RC) 16.7% case, the differences between the mean velocity profiles within and immediately above the canopy are hard to discern. The peak values of Reynolds shear stress for the higher packing density cases are all lower than the peaks for the lower packing density. This is because the flows over the flat roofed arrays falls into different flow regimes. At λ_p =16.7% the flow is in the early stages of the wake interference regime, while at λ_p =33.3% it is within the skimming regime. Figure 15 shows that the possible maximum drag coefficient is closer to $\lambda_p = 16.7\%$ than $\lambda_p = 33.3\%$ regardless the shape of roof, which is consistent with Cheng et al. (2007). It is crucial to note that the pitched roof increases the total drag coefficient substantially at the higher packing density $\lambda_p = 33.3\%$, whereas at the lower packing density $\lambda_p = 16.7\%$ the

effect of the roof on the drag coefficient is small. This confirms the observation in Sect. 6.1 that the pitched roof alters the flow regime at λ_p =33.3%, but it does not at λ_p = 16.7%. This suggests that the flow regime map against the packing density needs to be redrawn to take account of roof shape.

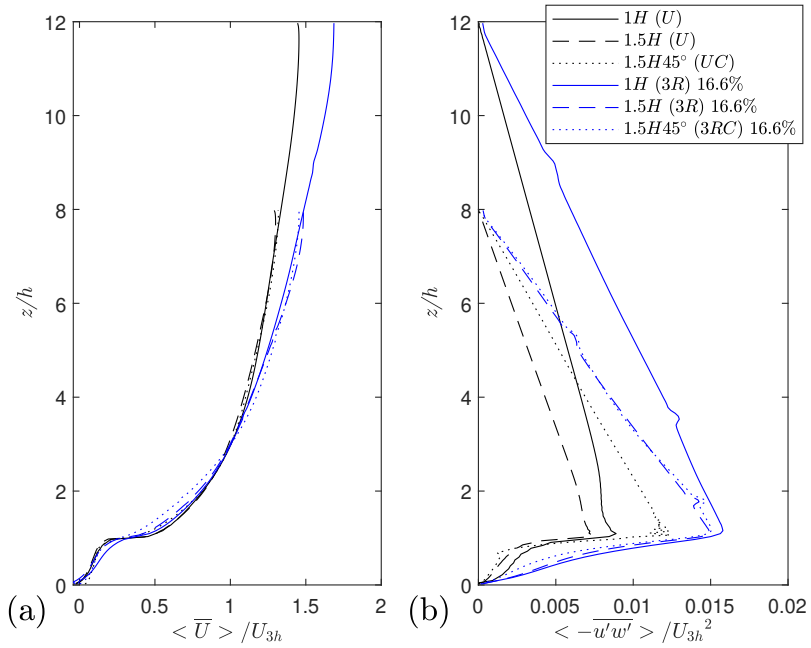

Fig. 15: Effects of packing density and roof shape on a) spatial- and time-averaged axial velocity profile, and b) spatial- and time-averaged Reynolds shear stress.

Figure 16 shows spatially-averaged mean streamwise velocity and Reynolds shear stress within and immediately above the canopy. The spatially-averaged mean velocity profiles are similar in shape, but the arrays with the lower packing density produce a smoother transition in the mean flow at the canopy top. As with the values above the canopy shown in Fig. 15, there is a clear difference in the values of Reynolds shear stress within the canopy for the two packing densities. It is noticeable though that the pitched roof reduces the Reynolds shear stress in most of the regions within the canopy, for both packing densities even though it substantially enhances the the Reynolds shear stress at the canopy height at λ_p = 33.3%. We speculate that the 45° slope on the windward side of the block convects most of the turbulence upwards and downstream, whereas the straight vertical windward side of the flat-roof blocks convects a large fraction of the turbulence downwards into a large circulation within the long street canyon as shown in Fig. 8.

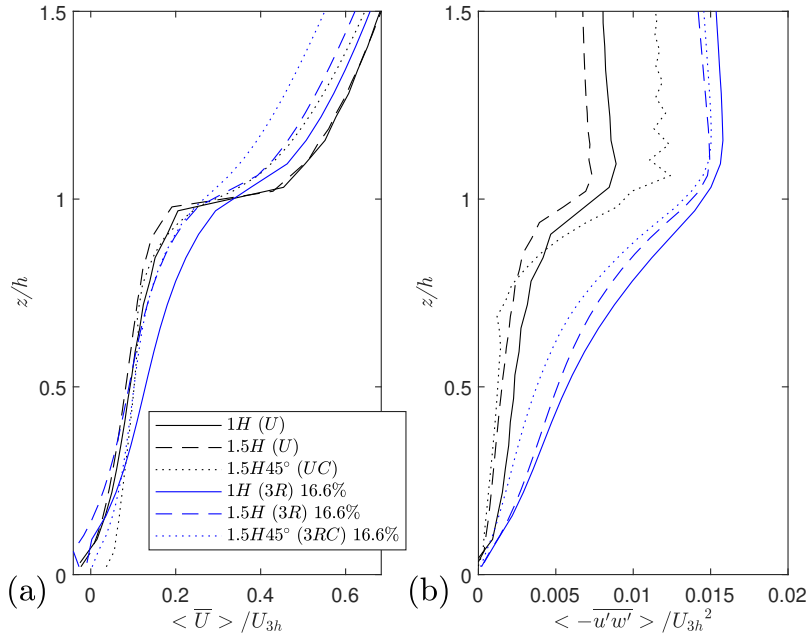

Fig. 16: Effects of packing density and and roof shape within the canopy on the a) spatial- and time-averaged axial velocity profile and the b) spatial- and time-averaged Reynolds shear stress.

7 Stratification Effects

The study of flow over pitched roofs in neutral conditions as shown previously is a crucial stepping stone, albeit that the occurrence of neutral atmospheric stability conditions is very rare. In this section the effects of stable stratification are examined for pitched-roof cuboids. Data from the STI domain is shown as laterally averaged vertical profiles at $x = 18.5H$, or spatially averaged between $17H - 19H$

Figure 17 shows the effects of stratification on the mean flow and turbulent statistics. The mean velocity profile is negligibly affected by all the stratification conditions analysed here. Sessa et al. (2018) drew the same conclusion for the mean flow over flat-roof cuboids. However, Figure17 shows an obvious effect of stratification on the turbulent statistics. The reduction of streamwise normal stress (Fig.17b) in going from $Ri = 0.2$ to $Ri = 0.5$ for the pitched roof case is approximately 7%, in contrast to a reduction of 25% for the flat-roof case (Sessa et al., 2018). For $Ri = 0.2$ and $Ri = 1$ the differences are 16% and 50% for the pitched and flat roof cases, respectively. Overall, the differences between the neutral and any of the stratified cases are far smaller for the pitched roof cuboids than for the flat-roof cases. This suggests that the flows created around pitched roof cuboids lead to a significant reduction in the effect of stable stratification conditions, when compared to predictions for flat-roof cuboids for the same inflow conditions.

In neutral conditions the flat-roof generates around 10% stronger streamwise fluctuations than the pitched roof, whereas it generates around 10% less vertical fluctuations than the pitched roof (see Fig.17 and Sessa et al. (2018)). This suggests that the pitched roof generates more three-dimensional turbulent eddies above the canopy, as opposed to the typical thin shear layers generated by the flat roof at the canopy height. The more energetic vertical turbulent fluctuations at the top of the pitched-roof cuboids reduce the stratification effect.

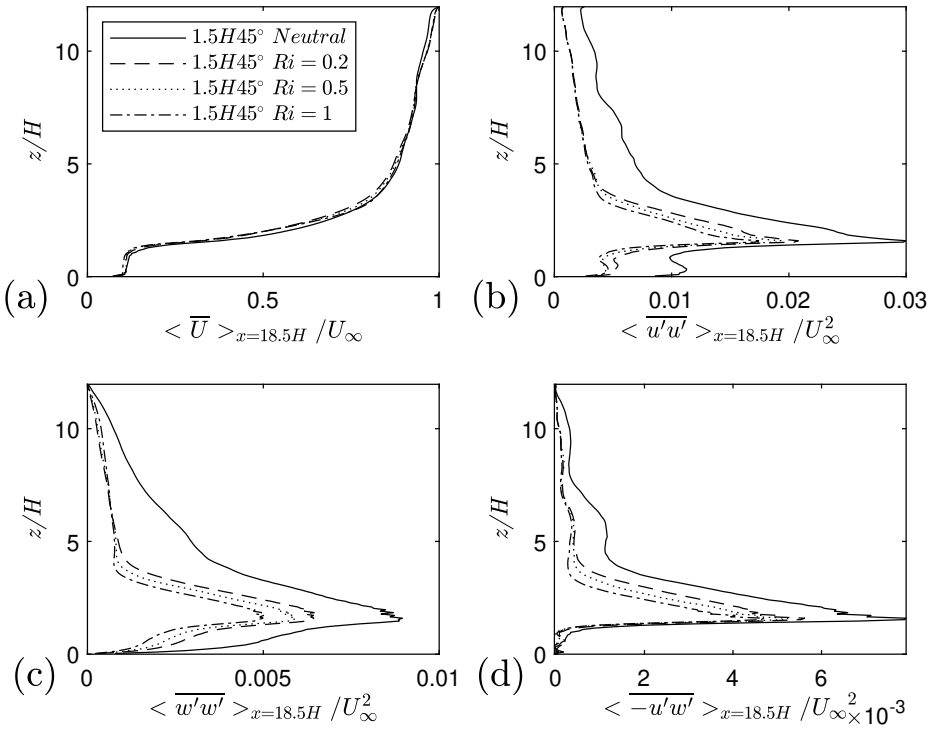

Fig. 17: Spanwise averaged data at $x = 18.5H$ for neutral and stratified conditions, $Ri = 0.2, 0.5, 1$, (a) mean velocity, (b) streamwise stress, (c) vertical stress and (d) Reynolds stress, normalised by the freestream velocity

Figure 18 shows contours of vertical fluctuations $\overline{w'w'}$ across a vertical plane located at $y = -1.5H$ (Fig. 3) for $Ri = 0$ and $Ri = 1$. It is clearly visible that the stable stratification reduces the strength of fluctuations across the entire fetch of the domain. Figure 18 also shows that the growth of the internal boundary layer is suppressed in the stratified flow. However, such a stratification effect is evidently less effective on suppressing the internal boundary layer compared to that over the flat-roof cuboids (Sessa et al., 2018), as we discussed in the preceding paragraph.

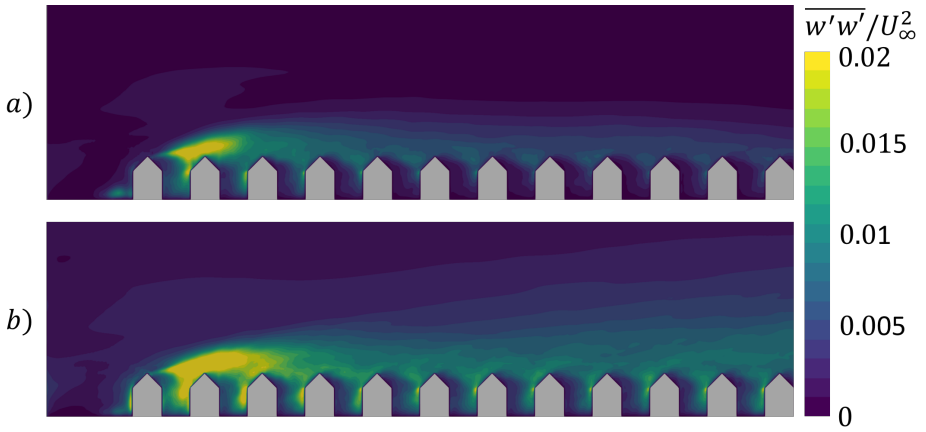

Fig. 18: Variance of vertical turbulent fluctuations normalised by freestream velocity for a) $Ri = 1$ and b) $Ri = 0$

8 Discussion

Holmes (2007) stated that surface loading was dependent on peak surface pressures. This suggests that the level of turbulence in the incoming flow is an important factor in surface loading. Based on this it is of interest to compare surface pressure coefficients calculated from the data produced here to values calculated from the Eurocode (En et al., 1991) which is used for estimating wind actions on structures, including pitched (gabled) roof buildings in urban or suburban environments.

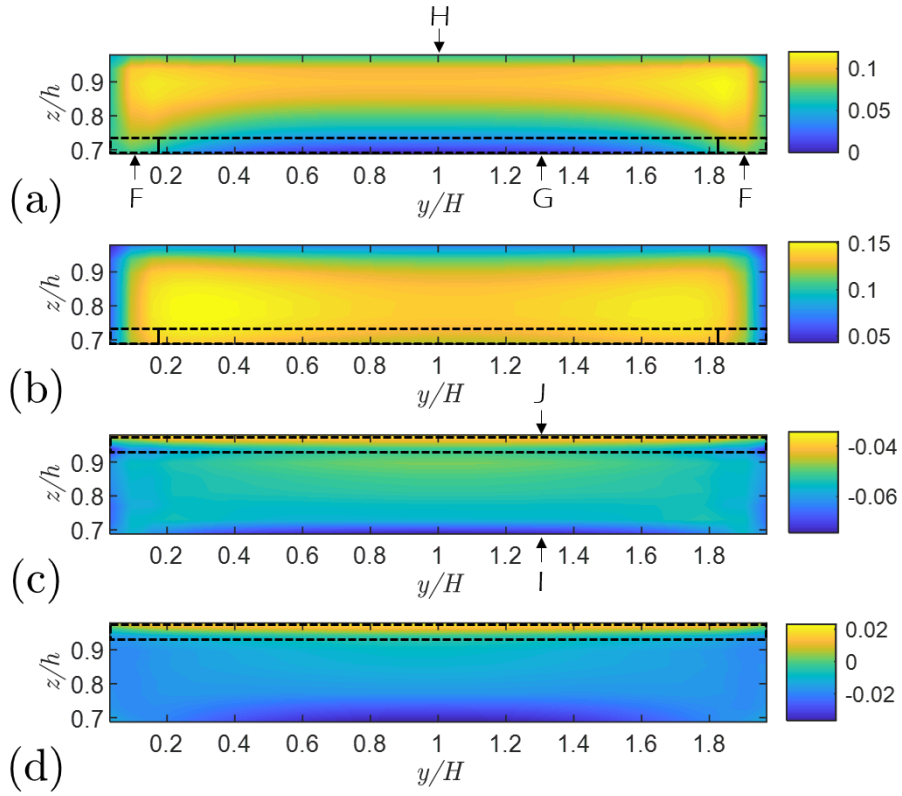

Fig. 19: Surface pressure coefficient for the windward side of (a) $\lambda_p = 33.3\%$ (b) $\lambda_p = 16.7\%$, and the leeward side of (c) $\lambda_p = 33.3\%$ and (d) $\lambda_p = 16.7\%$, demonstrating the regions for which wind loading can be calculated according to the Eurocode for wind actions, F, G, H for the windward side and J, I for the leeward side

The local surface pressure coefficient is calculated using Eq. 6,

$$Cp(t) = \frac{P(t) - P_0}{1/2\rho U_{\text{ref}}^2}, \tag{6}$$

where P_0 is the reference pressure, ρ is the density of air and U_{ref} is the time mean velocity, typically taken for low-rise buildings as the upstream velocity at the canopy top (Holmes, 2007). However, as PBC inflow conditions were used for these cases, U_{ref} was obtained following the method in Daniels et al. (2013) by fitting a power law with exponent 0.16, and a coefficient 2.675 to match the velocity profile with a freestream velocity U_∞ at the domain top. U_{ref} was then calculated at the canopy height $z = H$.

Figure 19 shows contour plots of surface pressure coefficient, as calculated using Eq. 6, for the two packing densities. To apply the Eurocode the surface area is

divided up regions F, G, H, I and J as indicated in Fig. 19. It is to be noted that scales of the colour bar are different in order to highlight the regions.

Even though the block geometries are the same there are obvious differences between the two surface pressure coefficient plots. Reducing the packing density and so increasing the distance causes the stagnation point to migrate down the windward roof - around 10% of the overall building height. In addition, the pressure on regions F, G and H increases as the distance between buildings increases because the windward roof is more exposed.

Figure 19c and d show a somewhat uniform pressure distribution on the leeward side roof, although slightly lower pressures are predicted on the leeward roof of the higher packing density case. This is likely to be due to a weakening of the street canyon type vortex, as it is 'stretched' further downstream, and confirms that in Bailey and Vincent (1943).

The Eurocode data (En et al., 1991) provided in Table 5 is for the most extreme load case of an isolated 45° pitched-roof building. It gives two sets of data for each of the 5 areas (see Fig. 19), and states "...four cases should be considered where the larges or smallest values of all areas F, G and H are combined with the largest or smallest values in areas I and J.". Table 5 only lists the largest values from the first set data of F, G and H, and the smallest values from the second set data of I and J. Other data are all zero.

Table 5 shows that surface pressure coefficients from the two LES cases are very different from the Eurocode data. This is for two reasons: firstly, the Eurocode data represent the possible extreme of surface pressure coefficients, estimation of which is outside the scope of this paper; secondly, Eurocode does not take the effect of sheltering by surrounding buildings into account. Table 5 shows substantial differences in the LES predicted average mean surface pressure on every area for the two packing density cases. This questions the applicability of an isolated-building standard for use in suburban or urban environments.

Table 5: Average mean surface pressure coefficient on the F, G and H areas of windward roof, and the I and J areas of leeward roof, mandated in the Eurocode (En et al., 1991). The table lists the largest values from the first set data of F, G and H, and the smallest values from the second set data of I and J, provided by (En et al., 1991).

Case Description	**F**	**G**	**H**	**I**	**J**
Eurocode	0.7	0.7	0.6	-0.2	-0.3
$1.5H45°(3RC)$ $\lambda_p = 33.3\%$	0.064	0.025	0.089	-0.045	-0.056
$1.5H45°(3RC)$ $\lambda_p = 16.7\%$	0.092	0.133	0.121	0.0068	-0.018

9 Conclusions

Large eddy simulations (LES) have been carried out to simulate the flow of urban boundary layers over idealized arrays of cuboids with and without pitched roofs, under neutral and stable stratification conditions. The reliability and accuracy of the results has been ensured by conducting rigorous evaluation tests, including examining mesh sensitivity and body conformity.

The results for a baseline flat roof cuboid array were first validated against previous data. The same mesh and numerical settings were then preserved as far as possible to ensure the reliability of flow simulations made for the 45° pitched roof cases.

The non-conformal Cartesian meshes used in some computational fluid dynamics codes, such as PALM and DALES, provide high computational efficiency but receive criticism with regard to their accuracy. This study has examined the accuracy of using this type of mesh and concluded that it produces acceptable mean flow and Reynolds stress predictions when compared to those from conformal (body-fitted) meshes.

Compared to that produced by an array of flat roof cuboids, introducing an array with 45° pitched roofs leads to significant changes in the mean flow field, the Reynolds stresses, and drag, and increases the turbulent momentum flux at the canopy height by approximately 50%. The magnitude of these changes strongly suggests that it is important to account for the effect of roof shape in urban arrays. In other words, the pitched roof array enhances the turbulent mixing and aerodynamic drag in a manner similar to having a random height array of flat-roofed cuboids (Xie et al., 2008).

The results have shown that the pitched roof case exhibits a different flow regime to that of the flat roof cases at packing density $\lambda_p = 33.3\%$. The pitched roof, due to decreased packing density in the top third of the canopy, is in the wake-interference regime, as apposed to the skimming flow regime experienced by the flat roof cuboids. At $\lambda_p = 16.7\%$ both the flat-roof and pitched roof cases are in the wake-interference regime. The normalised spatially averaged profiles of Reynolds stress over the flat- and pitched-roof buildings show a significantly smaller difference compared to at $\lambda_p = 33.3\%$. This suggests that the pitched roof only plays a crucial role within a certain range of packing densities.

Although pitched roof and random height arrays are more common than flat-roofed buildings of uniform height in urban areas, current parameterization schemes are typically based on arrays of uniform-height cuboids with flat roofs. The need for taking the effect of pitched roofs into account is given more importance by the fact that the results showed a much stronger effect for a packing density of around $\lambda_p = 33.3\%$ which is more common in suburban regions than $\lambda_p = 16.7\%$. The results suggest that omitting these effects in a high-resolution meso-scale models may introduce significant errors into boundary layer predictions over typical suburban and urban regions, where there are a high proportion of pitched roof or non-uniform height buildings.

It is also to be noted that our LES predictions showed considerable differences in mean surface pressure coefficient compared to values in the Eurocode estimation. While some of that was due to the Eurocode considering peak values, a substantial fraction is also attributable to the Eurocode not considering the sheilding effect of surrounding buildings which suggests that there is a need to consider for a more refined Eurocode to address this aspect.

Simulations showed that having pitched roofs meant that the effect of increasing stable stratification conditions ($0 \leq Ri \leq 1$) was very much reduced in comparison to the same incoming flow for flat roof cuboids. The relative difference in the vertical fluctuations between two weak stratification conditions $Ri = 0.2$ and $Ri = 1$ was around 16% less for the pitched roof cases, while a reduction of 50% was found for flat roof ones (Sessa et al., 2020). We conclude that pitched roofs

may greatly enhance the turbulent mixing in stable stratification conditions, and so improve the urban ventilation in the local environment. Consequently, pollution models which ignore the effects of pitched roofs may be overly pessimistic.

Acknowledgements

This research is mainly funded by a studentship of the Faculty of Engineering and the Environment. MC thanks Dr Tim Foat from Dstl for providing insight and support. Computational work has been undertaken on Southampton University's Iridis systems. The relevant data are available from the University of Southampton Institutional Repository, under https://doi.org/10.5258/SOTON/xxxxx(to be provided).

References

Badas MG, Ferrari S, Garau M, Querzoli G (2017) On the effect of gable roof on natural ventilation in two-dimensional urban canyons. J Wind Eng Ind Aerodyn 162:24–34

Bailey A, Vincent N (1943) Wind-pressure on buildings including effects of adjacent buildings. J Inst Civil Eng 20(8):243–275

Barlow J, Best M, Bohnenstengel SI, Clark P, Grimmond S, Lean H, Christen A, Emeis S, Haeffelin M, Harman IN, et al. (2017) Developing a research strategy to better understand, observe, and simulate urban atmospheric processes at kilometer to subkilometer scales. Bul Am Meteorol Soc 98(10):ES261–ES264

Barlow JF, Harman IN, Belcher SE (2004) Scalar fluxes from urban street canyons. part I: Laboratory simulation. Boundary-Layer Meteorol 113(3):369–385

Boppana V, Xie ZT, Castro I (2014) Thermal stratification effects on flow over a generic urban canopy. Boundary-Layer Meteorol 153(1):141–162

Castro IP (2017) Are urban-canopy velocity profiles exponential? Boundary-Layer Meteorol 164(3):337–351

Castro IP, Xie ZT, Fuka V, Robins AG, Carpentieri M, Hayden P, Hertwig D, Coceal O (2017) Measurements and computations of flow in an urban street system. Boundary-Layer Meteorol 162(2):207–230

Cheng H, Castro IP (2002) Near wall flow over urban-like roughness. Boundary-Layer Meteorol 104(2):229–259

Cheng H, Hayden P, Robins A, Castro I (2007) Flow over cube arrays of different packing densities. J Wind Eng Ind Aerodyn 95(8):715–740

Coceal O, Thomas T, Castro I, Belcher S (2006) Mean flow and turbulence statistics over groups of urban-like cubical obstacles. Boundary-Layer Meteorol 121(3):491–519

Daniels SJ, Castro IP, Xie ZT (2013) Peak loading and surface pressure fluctuations of a tall model building. J Wind Eng Ind Aerodyn 120:19–28

En B, et al. (1991) Eurocode 1: Actions on structures—part 1–4: General actions—wind actions. NA to BS EN, Brussels, Belgium

Fernando HJS (2010) Urban atmospheres in complex terrain. Annu Rev Fluid Mech 42:365–89

692 Ferrari S, Badas MG, Garau M, Seoni A, Querzoli G (2016) The air quality in
693 two-dimensional urban canyons with gable roof buildings: A numerical and lab-
694 oratory investigation. In: 17th Int Conf Harmonisation within Atmospheric Dis-
695 persion Modelling for Regulatory Purposes, HARMO 2016, Hungarian Meteo-
696 rological Service, vol 2016, pp 351–356
697 Fouad NS, Mahmoud GH, Nasr NE (2018) Comparative study of international
698 codes wind loads and CFD results for low rise buildings. Alexandria Eng J
699 57(4):3623–3639
700 Fuka V, Xie ZT, Castro IP, Hayden P, Carpentieri M, Robins AG (2018) Scalar
701 fluxes near a tall building in an aligned array of rectangular buildings. Boundary-
702 Layer Meteorol 167(1):53–76
703 Ginger J, Letchford C (1995) Pressure factors for edge regions on low rise building
704 roofs. J Wind Eng Ind Aerodyn 54:337–344
705 Grylls T, Suter I, van Reeuwijk M (2020) Steady-state large-eddy simulations
706 of convective and stable urban boundary layers. Boundary-Layer Meteorol
707 175(3):309–341
708 Han BS, Park SB, Baik JJ, Park J, Kwak KH (2017) Large-eddy simulation of vor-
709 tex streets and pollutant dispersion behind high-rise buildings. Q J R Meteorol
710 Soc 143(708):2714–2726
711 Hanna S, Tehranian S, Carissimo B, Macdonald R, Lohner R (2002) Comparisons
712 of model simulations with observations of mean flow and turbulence within
713 simple obstacle arrays. Atmos Environ 36(32):5067–5079
714 Hertwig D, Gough HL, Grimmond S, Barlow JF, Kent CW, Lin WE, Robins
715 AG, Hayden P (2019) Wake characteristics of tall buildings in a realistic urban
716 canopy. Boundary-Layer Meteorol 172(2):239–270
717 Heus T, van Heerwaarden CC, Jonker HJJ, Pier Siebesma A, Axelsen S, van den
718 Dries K, Geoffroy O, Moene AF, Pino D, de Roode SR, Vilà-Guerau de Arellano
719 J (2010) Formulation of the dutch atmospheric large-eddy simulation (dales) and
720 overview of its applications. Geosci Model Dev 3(2):415–444, DOI 10.5194/gmd-
721 3-415-2010
722 Holmes J (1994) Wind pressures on tropical housing. J Wind Eng Ind Aerodyn
723 53(1–2):105–123
724 Holmes JD (2007) Wind loading of structures. CRC press
725 Inagaki M, Kondoh T, Nagano Y (2005) A mixed-time-scale sgs model with fixed
726 model-parameters for practical les. J Fluids Eng 127(1):1–13
727 Kanda I, Yamao Y (2016) Passive scalar diffusion in and above urban-like rough-
728 ness under weakly stable and unstable thermal stratification conditions. J Wind
729 Eng Ind Aerodyn 148:18–33
730 Kanda M, Moriwaki R, Kasamatsu F (2004) Large-eddy simulation of turbulent
731 organized structures within and above explicitly resolved cube arrays. Boundary-
732 Layer Meteorol 112(2):343–368
733 Krč P, Resler J, Sühring M, Schubert S, Salim MH, Fuka V (2020) Radiative
734 transfer model 3.0 integrated into the PALM model system 6.0. Geosci Model
735 Dev pp 1–41
736 Llaguno-Munitxa M, Bou-Zeid E, Hultmark M (2017) The influence of building
737 geometry on street canyon air flow: validation of large eddy simulations against
738 wind tunnel experiments. J Wind Eng Ind Aerodyn 165:115–130
739 Maronga B, Banzhaf S, Burmeister C, Esch T, Forkel R, Fröhlich D, Fuka V,
740 Gehrke KF, Geletič J, Giersch S, Gronemeier T, Groß G, Heldens W, Hell-

741 sten A, Hoffmann F, Inagaki A, Kadasch E, Kanani-Sühring F, Ketelsen K,
742 Khan BA, Knigge C, Knoop H, Krč P, Kurppa M, Maamari H, Matzarakis A,
743 Mauder M, Pallasch M, Pavlik D, Pfafferott J, Resler J, Rissmann S, Russo
744 E, Salim M, Schrempf M, Schwenkel J, Seckmeyer G, Schubert S, Sühring M,
745 von Tils R, Vollmer L, Ward S, Witha B, Wurps H, Zeidler J, Raasch S (2020)
746 Overview of the palm model system 6.0. Geosci Model Dev 13(3):1335–1372,
747 DOI 10.5194/gmd-13-1335-2020
748 Marucci D, Carpentieri M (2020) Dispersion in an array of buildings in stable and
749 convective atmospheric conditions. Atmos Environ 222:117,100
750 Marucci D, Carpentieri M, Hayden P (2018) On the simulation of thick non-
751 neutral boundary layers for urban studies in a wind tunnel. Int J Heat Fluid
752 Flow 72:37–51
753 Nosek Š, Kukačka L, Kellnerová R, Jurčáková K, Jaňour Z (2016) Ventila-
754 tion processes in a three-dimensional street canyon. Boundary-Layer Meteorol
755 159(2):259–284
756 Nosek Š, Kukačka L, Jurčáková K, Kellnerová R, Jaňour Z (2017) Impact of roof
757 height non-uniformity on pollutant transport between a street canyon and in-
758 tersections. Environ Pollut 227:125–138
759 Oliveira PJ, Younis BA (2000) On the prediction of turbulent flows around full-
760 scale buildings. J Wind Eng Ind Aerodyn 86(2-3):203–220
761 Ozmen Y, Baydar E, Van Beeck J (2016) Wind flow over the low-rise building
762 models with gabled roofs having different pitch angles. Build Environ 95:63–74
763 Placidi M, Ganapathisubramani B (2015) Effects of frontal and plan solidities
764 on aerodynamic parameters and the roughness sublayer in turbulent boundary
765 layers. J Fluid Mech 782:541–566
766 Placidi M, Ganapathisubramani B (2018) Turbulent flow over large roughness
767 elements: effect of frontal and plan solidity on turbulence statistics and structure.
768 Boundary-Layer Meteorol 167(1):99–121
769 Sessa V, Xie ZT, Herring S (2018) Turbulence and dispersion below and above
770 the interface of the internal and the external boundary layers. J Wind Eng Ind
771 Aerodyn 182:189–201
772 Sessa V, Xie ZT, Herring S (2020) Thermal stratification effects on turbulence and
773 dispersion in internal and external boundary layers. Boundary-Layer Meteorol
774 176(1):61–83
775 Stoesser T, Mathey F, Frohlich J, Rodi W (2003) Les of flow over multiple cubes.
776 Ercoftac Bulletin 56:15–19
777 Tomas J, Pourquie M, Jonker H (2016) Stable stratification effects on flow and
778 pollutant dispersion in boundary layers entering a generic urban environment.
779 Boundary-Layer Meteorol 159(2):221–239
780 Tomas JM, Eisma HE, Pourquie MJBM, Elsinga GE, Jonker HJJ, Westerweel J
781 (2017) Pollutant dispersion in boundary layers exposed to rural-to-urban tran-
782 sitions: Varying the spanwise length scale of the roughness. Boundary-Layer
783 Meteorol 163:225–251, DOI https://doi.org/10.1007/s10546-016-0226-x
784 Tominaga Y, Akabayashi Si, Kitahara T, Arinami Y (2015) Air flow around iso-
785 lated gable-roof buildings with different roof pitches: Wind tunnel experiments
786 and cfd simulations. Build Environ 84:204–213
787 Tsutsumi J, Katayama T, Nishida M (1992) Wind tunnel tests of wind pressure
788 on regularly aligned buildings. J Wind Eng Ind Aerodyn 43(1-3):1799–1810

789 Vanderwel C, Ganapathisubramani B (2015) Effects of spanwise spacing on large-
790 scale secondary flows in rough-wall turbulent boundary layers. J Fluid Mech
791 774:R2, DOI 10.1017/jfm.2015.292
792 Willingham D, Anderson W, Christensen KT, Barros JM (2014) Turbulent
793 boundary layer flow over transverse aerodynamic roughness transitions: In-
794 duced mixing and flow characterization. Phys Fluids 26(2):025,111, DOI
795 10.1063/1.4864105
796 Woodward H, Gallacher D, Robins AG, ApSimon H (2021) A review of the ap-
797 plicability of gaussian modelling techniques to near-field dispersion. In: Pub-
798 lications of the ADMLC, Atmospheric Dispersion Modelling Liaison Commit-
799 tee, admlc.files.wordpress.com/2021/01/short_range_gaussian_finalised1.pdf, vol
800 ADMLC-R11, pp 1–79
801 Xie ZT, Castro IP (2006) LES and RANS for turbulent flow over arrays of wall-
802 mounted obstacles. Flow Turbul and Combust 76(3):291
803 Xie ZT, Castro IP (2008) Efficient generation of inflow conditions for large eddy
804 simulation of street-scale flows. Flow Turbul Combust 81(3):449–470
805 Xie ZT, Castro IP (2009) Large-eddy simulation for flow and dispersion in urban
806 streets. Atmos Environ 43(13):2174–2185
807 Xie ZT, Fuka V (2018) A note on spatial averaging and shear stresses within urban
808 canopies. Boundary-Layer Meteorol 167(1):171–179
809 Xie ZT, Coceal O, Castro IP (2008) Large-eddy simulation of flows over random
810 urban-like obstacles. Boundary-Layer Meteorol 129(1)
811 Xie ZT, Hayden P, Wood CR (2013) Large-eddy simulation of approaching-flow
812 stratification on dispersion over arrays of buildings. Atmos Environ 71:64–74
813 Yassin MF (2011) Impact of height and shape of building roof on air quality in
814 urban street canyons. Atmos Environ 45(29):5220–5229